The direct exchange mechanism of induced spin polarization of low-dimensional π-conjugated carbon- and *h*-BN fragments at LSMO(001) MnO-terminated interfaces

Artem V. Kuklin[a,b], Alexander A. Kuzubov[b,c], Evgenia A. Kovaleva[b,c], Hyosun Lee[a], Pavel B. Sorokin[e], Seiji Sakai[d], Shiro Entani[d], Hiroshi Naramoto[d], and Paul Avramov[a,*]

[a]*Department of Chemistry and* ***Green-Nano Materials Research Center,*** *Kyungpook National University, 80 Daehak-ro, Buk-gu, Daegu, 41566, Republic of Korea*
[b]*Siberian Federal University, 79 Svobodniy pr., Krasnoyarsk 660041, Russia*
[c]*L.V. Kirensky Institute of Physics SB RAS, 50/38 Akademgorodok, Krasnoyarsk 660036, Russia*
[d]*National Institutes for Quantum and Radiological Science and Technology QST, Tokai, Naka, Ibaraki 319-1195, Japan*
[e]*National University of Science and Technology MISiS, Moscow, 119049, Russian Federation*

Induced spin polarization of π-conjugated carbon and *h*-BN low dimensional fragments at the interfaces formed by deposition of pentacene molecule and narrow zigzag graphene and *h*-BN nanoribbons on MnO_2-terminated LSMO(001) thin film was studied using GGA PBE+U PAW D3-corrected approach. Induced spin polarization of π-conjugated low-dimensional fragments is caused by direct exchange with Mn ions of LSMO(001) MnO-derived surface. Due to direct exchange, the pentacene molecule changes its diamagnetic narrow-band gap semiconducting nature to the ferromagnetic semiconducting state with 0.15 eV energy shift between spin-up and spin-down valence bands and total magnetic moment of 0.11 μ_B. Direct exchange converts graphene nanoribbon to 100% spin-polarized half-metal with large amplitude of spin-up electronic density at the Fermi level. The direct exchange narrows the *h*-BN nanoribbon band gap from 4.04 eV to 1.72 eV in spin-up channel and converts the *h*-BN ribbon semiconducting diamagnetic nature to a semiconducting magnetic one. The electronic structure calculations demonstrate a possibility to control the spin properties of low-dimensional π-conjugated carbon and *h*-BN fragments by direct exchange with MnO-derived LSMO(001) surface for spin-related applications.

* To whom correspondence should be addressed.

E-mail: paul@iph.krasn.ru

Keywords: Graphene nanoribbons, DFT, LSMO thin films, induced spin polarization, *h*-BN nanoribbons, half-metal.

Introduction

The roles of indirect and double exchange interactions in manganites was elucidated in several experimental and theoretical publications (see, for example [1,2]). In particular [2], it was found that magnetism of $La_{0.9}Sr_{0.1}Mn_{1-x}Ga_xO_{3+\gamma}$ is caused by Ruderman, Kittel, Kasuya, Yosida (RKKY, [3–5]) mechanism of indirect exchange. Using photoemission and X-ray spectroscopy it was found that in $La_{1-x}Sr_xMnO_3$ ($0.2 \le x \le 0.6$) the oxygen holes are antiferromagnetically bounded with high spin configurations of Mn^{3+} ions [6,7]. The electron-hole excitation leads to charge transfer from O2*p* subband to Mn^{3+} ion with the formation of Mn^{4+} configuration through double exchange mechanism [8]. The LDA electronic structure calculations [9] confirmed the experimental results revealing strong hybridization of Mn*d*- and O2*p* subbands.

In recent years, carbon-based materials attract much attention as promising building blocks for spintronic applications[10–12] because of their extremely high mobility of electrons together with long spin transport length[13,14] caused by weak spin-orbit interactions of carbon atoms. Such remarkable properties allow one to design graphene-based spintronic and spincaloritronic nanodevices.

Many ferromagnetic supports cause strong induced spin polarization of deposited π-conjugated organic media [15,16]. with high magnetoresistance [17,18]. Perovskite manganites are well known as an advantage class of functional with rich variety of magnetic and electric properties, such as half-metallic ferromagnetism, high magnetoresistance, perfect spin polarization and charge/orbital ordering [19–21]. Half-metallic $La_{1-x}Sr_xMnO_3$ (LSMO), which is characterized by colossal magnetoresistance, low-density of charge carriers, high Curie temperature and partial transparency [21,22] is one of the most promising materials for magnetic tunnel junctions and effective spin injection in graphene and related π-conjugated organic media. The role of surface magnetization of LSMO was underlined in Refs. [22–24] and it was shown that in the LSMO/Alq_3/Co magnetic tunnel junction, which exhibits magnetoresistance up to 300%, the interfacial spin-dependent metal-organic media hybridization causes an enhancement and even a sign reversal of injected spins. It was also found that the coupling of the electronic states of graphene with Mn ions is very high [25]. The unique magnetic properties of LSMO allow one to develop spin-polarized organic light emitting diodes [26,27] and spin-valve [28,29]. nanodevices. Another example is a spin valve device consisting of carbon nanotube deposited on $La_{0.7}Sr_{0.3}MnO_3$ electrodes[30], which demonstrates a long spin lifetime and high Fermi velocity in the nanotube. Recent photoemission study of the evolution of the electronic structure at C_{60}/LSMO exhibits 0.61 eV interface barrier for the electrons to be injected from LSMO to C_{60}[31].

Due to the long spin lifetime of charge carriers, π-conjugated organic media is considered as promising materials for spintronics nanodevices [32,33] and pentacene molecule $C_{22}H_{14}$ is one of them. This highly conjugated organic molecule exhibits semiconducting electronic properties due to the narrow HOMO-LUMO gap and exciton generation upon absorption of ultra-violet or visible light. It was demonstrated that vertical pentacene-based spintronic devices with $La_{0.7}Sr_{0.3}MnO_3$ and Co electrodes retain magnetoresistive effects up to room temperature [34]. Pentacene binds with Au substrate by weak van der Waals interactions, while Cu and Ag substrates cause chemical interfragment bonding [35]. Recently, spin-dependent molecular symmetries associated with *p–d* hybridization between pentacene and cobalt nanoscale islands deposited on Cu(111) was studied by SP-STM technique [36]. which allows to predict and control induced spin polarization of π-conjugated molecule on magnetic substrates.

Zigzag *h*-BN (ZBNNRs) [37,38] and graphene nanoribbons (ZGNRs) are other examples of the key π-conjugated media to promote spin injection through tunneling junctions, chemical passivation and create insulating layers. It was shown that ZGNRs are antiferromagnetic semiconductors [39] with ferromagnetic spin ordering at each edge [40–42]. Zigzag graphene nanoribbons can be used in spintronics as spin-FET [43] spin logic gates and spin filtering devices [42]. A new highly efficient spin caloritronics MR devices can be fabricated using ZGNR with heterojunctions consisting of single (or double) hydrogen-terminated ZGNR [44]. It is worth to note that ZGNRs demonstrate single-channel room temperature ballistic conductivity on a length scale equal to ten micrometers, which is greater the theoretically predicted value for perfect graphene [45,46]. The unique properties of graphene nanoribbons open unique possibility to create novel LSMO-based heterostructures with induced half-metallic ferromagnetic nature for promising spintronics and spincaloritronics applications.

In this paper, the mechanism of induced spin polarization of pentacene, narrow zigzag graphene and *h*-BN nanoribbons at the interfaces through the direct exchange with MnO_2-terminated LSMO(001) thin film was studied by electronic structure calculations. The surface induces asymmetry causes formation of 2D electron gas localized at the interfaces and lift of spin degeneracy of low-dimensional fragments. The types of coordination of the fragments, the nature of bonding, the degrees of spin polarization of low-dimensional π-conjugated carbon and *h*-BN fragments are predicted and theoretically studied. It was found that weak dispersion forces determine the nature and energy of bonding between the fragments and LSMO(001) substrate.

Computational Methods

To run all electronic structure calculations of pentacene, graphene- and *h*-BN zigzag nanoribbons deposited on MnO_2-terminated LSMO(001) surface, *ab initio* Density Functional Theory (DFT) within the projector augmented wave (PAW) [47] method and GGA+U [48,49] exchange-correlation functional proposed by Perdew, Burke and Ernzerhof (PBE) [50] were used. The empirical D3 Grimme corrections [51] and periodic boundary conditions (PBC) was employed. The $U = 2$ and $J = 0.7$ eV parameters and cutoff energy $E_{cutoff} = 450$ eV were adopted from earlier LSMO calculations [52–54]. For unit cell calculation the Brillouin zone reciprocal space was sampled by $12 \times 12 \times 12$ *k*-points using Monkhorst-Pack scheme [55]. To perform all electronic structure calculations, VASP code was used [56,57]. The electronic structure calculations of bulk $La_{0.67}Sr_{0.33}MnO_3$ reveal *a* translation vector equal to 3.886 Å which is in a good agreement with experimental data ($a = 3.876$ Å [58] and $a = 3.87$ Å [59]) and previous theoretical calculations ($a = 3.89$ Å [52]).

The atomic structure of $La_{0.67}Sr_{0.33}MnO_3$ is presented in Figure 1. Following the experimental data [60–65], the MnO_2 terminal layer could be employed to design the slab model of LSMO(001) thin film to introduce direct exchange mechanism for induced spin polarization of low-dimensional π-conjugated nanofragments. The structure of LSMO(001) contains six layers: one SrO layer formed by tetrahedrally coordinated Sr ions on the bottom of the plate, two MnO layers formed by octahedrally coordinated Mn ions, one top surface MnO layer formed by MnO_5 pyramids and two LaO layers formed by tetrahedral La ions. The La and Sr ions occupy the centers of the cubes formed by Mn ions.

To simulate the LSMO(001)-based heterostructures zigzag graphene and *h*-BN nanoribbons were used as well as highly conjugated pentacene molecule ($C_{22}H_{14}$, five linearly-fused benzene rings). The supercells of narrow zigzag graphene and *h*-BN nanoribbons consist of three C_6 or B_3N_3 hexagons in width and three hexagons in length ($C_{24}H_6$ and $B_{12}N_{12}H_6$

supercells) with standard notations 4-ZGNR and 4-ZBNNR, respectively. Since the Mn ions make dominant contribution to the magnetic properties of LSMO and provide a high degree of induced spin polarization of low-dimensional π-conjugated fragments, the MnO-terminated LSMO(001) surface was used to design low-dimensional heterostructures, namely pentacene/LSMO(001), 4-ZGNR/LSMO(001) and 4-ZBNNR/LSMO(001). The 5×2×1 ($La_{20}Sr_{10}Mn_{30}O_{90}$) and 8×2×1 ($La_{32}Sr_{16}Mn_{48}O_{144}$) supercells were used to simulate the pentacene/LSMO(001) and 4-ZGNR/LSMO(001) and 4-ZBNNR/LSMO(001) heterostructures, respectively. To avoid artificial interactions between the supercell images, the vacuum interval of 17 Å along *c* direction was used. 2×6×1 and 1×6×1 Γ-centered Monkhorst-Pack *k*-point Brillouin zone sampling scheme were set to calculate the atomic and electronic structure of pentacene/LSMO(001) and 4-ZGNR (4-ZBNNR)/LSMO(001) composites, respectively.

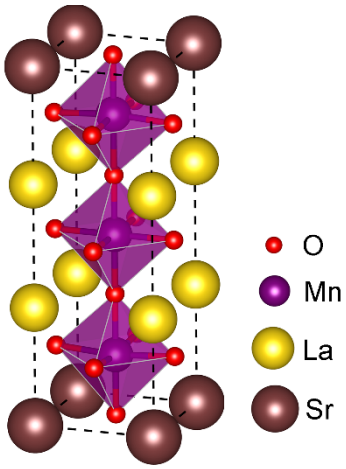

Figure 1. Atomic structure of $La_{0.67}Sr_{0.33}MnO_3$. The oxygen, manganese, lanthanum and strontium atoms are presented in red, purple, yellow and grey-pink respectively.

The cohesive energies of 4-ZGNR, pentacene and 4-ZBNNR with LSMO(001) thin film substrate were calculated using the following equation:

$$E_C = E_T \quad E_{LSMO} \quad E_{frag}$$

where E_T is the total energy of the composites, E_{LSMO} is the energy of pristine LSMO slab and E_{frag} is the energy of freestanding low-dimension fragment, either 4-ZGNR, pentacene molecule or 4-ZBNNR.

To define coordination types of 4-ZGNR, 4-ZBNNR and pentacene on MnO-terminated layer, standard notations of coordination sites (η^1, η^2, η^3 and η^6) are used throughout the text to denote the coordination of Mn ions to a single atom (η^1), middle of C-C and B-N bonds (η^2), C_3, BN_2 and NB_2 triangles (η^3) and middle of C_6 and B_3N_3 hexagons (η^6) of the low-dimensional carbon- and *h*-BN nanofragments.

Results and Discussion

The electronic structure calculations of all LSMO slabs reveal small rotations of MnO_6 octahedrons which coincide well with previous experimental [66] and theoretical [67] publications. The interaction of 2D fragments with LSMO leads to visible modifications of the

atomic and electronic structure of the constituent low-dimensional parts, like curvature of the nanofragments and substrate top layers.

a) Structure and energetic stability of pentacene/LSMO(001) interface

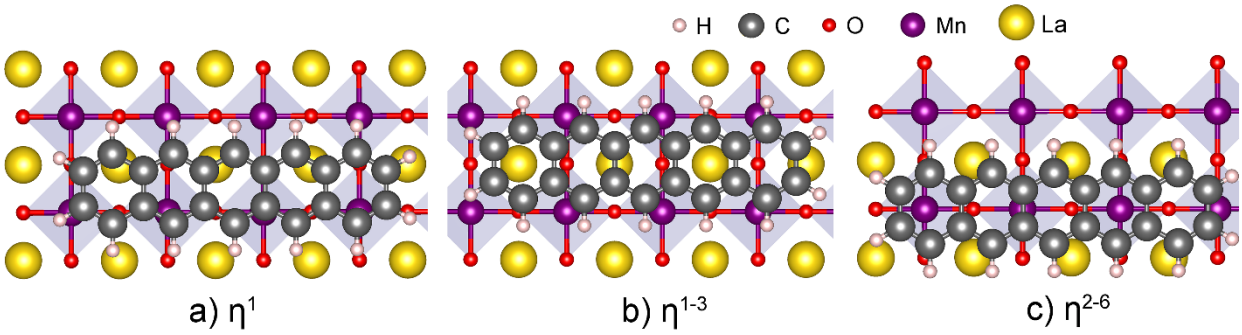

Figure 2. Pentacene/LSMO(001) interfaces. (a), (b) and (c) are η^{1}, η^{1-3} and η^{2-6} configurations, respectively.

Three possible configurations of pentacene on MnO-terminated (001) surface of LSMO thin film (Figure 2, Table 1) were revealed, namely: a) η^{1}; b) η^{1-3} and c) η^{2-6}. The first η^{1} configuration is characterized by Mn ions coordinated atop C atom (Figure 2a). The second η^{1-3} is characterized by coordination of Mn ions to C atoms and C_3 fragments (Figure 2b). Pentacene molecule in the third η^{2-6} configuration (Figure 2c) is coordinated by Mn ions through the middle of C-C bonds and C_6 hexagon. The η^{1-3} configuration is energetically preferable among all three heterostructures with almost the same interplanar distances (3.240 – 3.250 Å).

Table 1. Cohesive energies and interplanar distances of pentacene/LSMO(001) composite

Configuration	η^{1}	η^{1-3}	η^{2-6}
Cohesive energy, eV/supercell (Cohesive energy, eV/carbon atom)	–1.848 (–0.084)	–1.900 (–0.086)	–1.838 (–0.083)
Average interplanar distance, Å	3.240	3.242	3.250

b) Structure and energetic stability of 4-ZGNR/LSMO(001) interface

Three possible 4-ZGNR/LSMO(001) interfaces (Figure 3, Table 2), namely $\eta^{1-2-3-6}$ (Figures 3a), η^{1} (Figures 3b) and η^{3} (Figures 3c) were revealed and studied using the electronic structure calculations. As in the case of pentacene/LSMO(001) heterostructure, energetically preferable $\eta^{1-2-3-6}$ configuration has both η^{1} and η^{3} coordinations of surface Mn ions to hexagonal carbon lattice. Two other positions (η^{1} and η^{3}) are energetically metastable. The $\eta^{1-2-3-6}$ configuration is characterized by 2.892 Å distance between LSMO and 4-ZGNR fragments, which is significantly shorter than pentacene – MnO interplanar distance of 3.242 Å, and smaller cohesive energy per carbon atom (–0.011 eV/carbon atom) in comparison with –0.086 eV/carbon atom (Table 1) for pentacene.

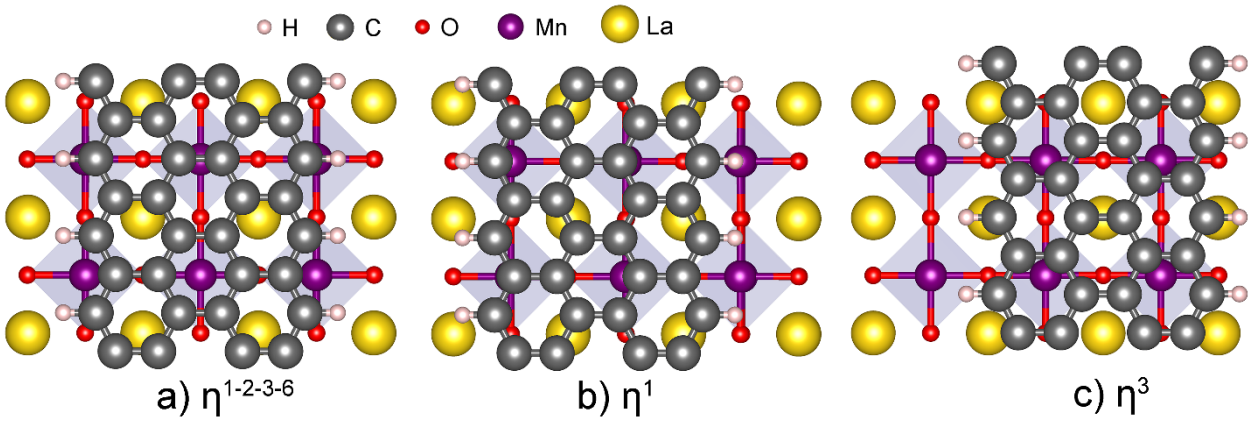

Figure 3. 4-ZGNR/LSMO(001) interface. (a), (b) and (c) are $\eta^{1\text{-}2\text{-}3\text{-}6}$, η^{1} and η^{3} configurations, respectively.

Table 2. Cohesive energies and interplanar distances of 4-ZGNR/LSMO(001) composites

Configuration	$\eta^{1\text{-}2\text{-}3\text{-}6}$	η^{1}	η^{3}
Cohesive energy, eV/supercell	–0.263	0.022	0.292
(Cohesive energy, eV/carbon atom)	(–0.011)	(0.001)	(0.012)
Average interplanar distance, Å	2.892	2.830	2.985

c) Structure and energetic stability of 4-ZBNNR/LSMO(001) interface

Similarly to 4-ZGNR heterostructure, the most preferable configuration of 4-ZBNNR (Table 3, Figure 4b) is $\eta^{1\text{-}2\text{-}3\text{-}6}$. The cohesive energies per BN pair of all 4-ZBNNR configurations are much stronger than the energies per carbon dimer for 4-ZGNR (Table 2, Figure 3). The interplanar distances for 4-ZBNNR on LSMO are equal to 2.873 – 3.093 Å, which is comparable to those for 4-ZGNR and relatively smaller than interplanar distances for pentacene/LSMO(001). The stronger bonding and shorter distances between the 4-ZBNNR and MnO-terminated LSMO(001) thin film in comparison with 4-ZGNR/LSMO(001) heterostructure could be explained by attractive electrostatic interactions between LSMO(001) surface Mn and O ions and positively (B) and negatively (N) charged atoms of *h*-BN.

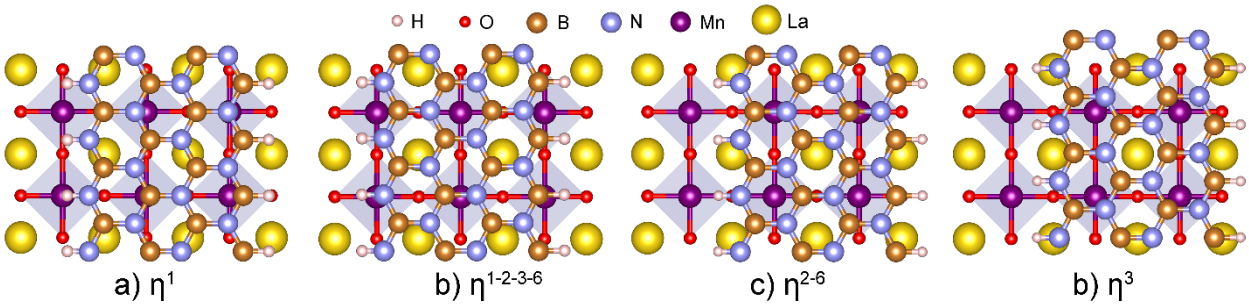

Figure 4. 4-ZBNNR/LSMO(001) interface. (a), (b) and (c) are η^{1}, $\eta^{1\text{-}2\text{-}3\text{-}6}$, $\eta^{2\text{-}6}$ and η^{3} configurations.

Table 3. Cohesive energies and interlayer distances of 4-ZBNNR/LSMO(001) composites

Configuration	η^1	$\eta^{1\text{-}2\text{-}3\text{-}6}$	$\eta^{2\text{-}6}$	η^3
Cohesive energy, eV/supercell (Cohesive energy, eV/BN pair)	–1.585 (–0.132)	–1.724 (–0.144)	–1.596 (–0.133)	–1.647 (–0.137)
Average interplanar distance, Å	2.873	2.873	2.880	3.093

The binding energies of energetically favorable configurations of pentacene/LSMO(001), 4-ZGNR/LSMO(001) and 4-ZBNNR/LSMO(001) heterostructures are very close to the upper limit of van der Waals (vdW) energy, which indicates negligible role of chemical binding (either covalent, complex or ionic) between LSMO and low-dimensional nanofragments. For all heterostructures η^1 and η^3 coordinations are responsible for formation of the most stable interfaces (Tables 1-3), which is not typical for complex compounds of *d*-elements with π-conjugated ligands.

d) Electronic structure of pentacene, 4-ZGNR and 4-ZBNNR deposited on MnO-terminated LSMO(001) surface

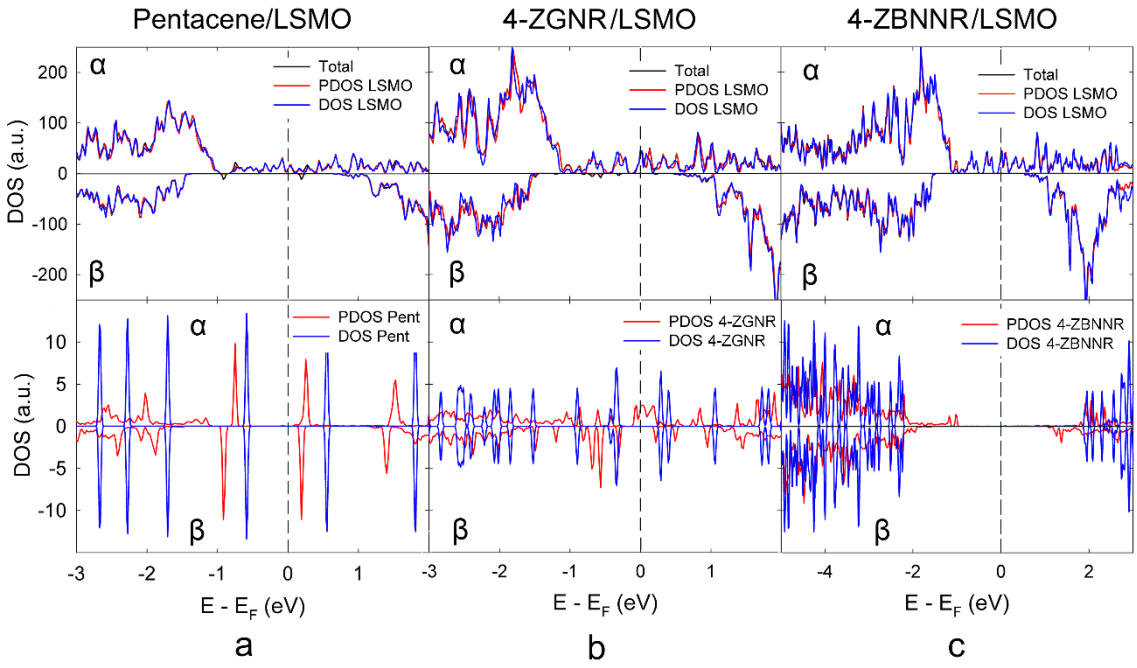

Figure 5. Total and partial density of states of energetically preferable (a) $\eta^{1\text{-}3}$ configuration of pentacene/LSMO(001), (b) $\eta^{1\text{-}2\text{-}3\text{-}6}$ configuration of 4-ZGNR/LSMO(001), and (c) $\eta^{1\text{-}2\text{-}3\text{-}6}$ configuration of 4-ZBNNR/LSMO(001) heterostructures.

Total and partial density of states of pentacene/LSMO(001) ($\eta^{1\text{-}3}$ configuration), 4-ZGNR/LSMO(001) ($\eta^{1\text{-}2\text{-}3\text{-}6}$) and 4-ZBNNR/LSMO(001) ($\eta^{1\text{-}2\text{-}3\text{-}6}$) are presented in Figure 5. All heterostructures are half-metals due to the major contribution of half-metallic LSMO thin film support to the electronic properties of the composites. The $\eta^{1\text{-}2\text{-}3\text{-}6}$ configuration of 4-ZGNR/LSMO(001) demonstrate 100% spin polarization of 4-ZGNR with large spin-up PDOS at

the Fermi level. At the same time, pentacene and 4-ZBNNR fragments exhibit visible spin-up and spin-down PDOS energy splitting caused by the lift of spin-degeneracy. The freestanding pentacene molecule has diamagnetic closed-shell electronic structure with HOMO-LUMO gap equal to 0.9 eV (Figure 5a). Direct exchange interactions with LSMO cause narrowing of the spin-up HOMO-LUMO gap up to 0.75 eV with keeping spin-down band gap intact, which leads to 0.15 eV shift of both spin-down HOMO and LUMO states towards low energy region. The total magnetic moment of pentacene in pentacene/LSMO(001) heterostructure is become equal to 0.11 μ_B. Near the Fermi level, PDOS of pentacene fragment is characterized by weak dispersion due to its quasi-molecular nature of the electronic states.

The direct exchange interactions of LSMO electronic subsystem with antiferromagnetic 4-ZGNR generate 100% spin-up polarization of the fragment with spin-down valence band maximum (VBM) – conduction band minimum (CBM) gap equal to 0.44 eV (Figure 5b). The spin polarization of 4-ZGNR follows positive sign of the substrate. The preservation of spin polarization sign shows that the spin transport in the 4-ZGNR/LSMO composite should be strong.[67] Since LSMO exhibits colossal magnetoresistance, the organic spin valves based on LSMO should also carry large MR.

Freestanding diamagnetic 4-ZBNNR is characterized by wide band gap (4.04 eV, Figure 5c). The unique magnetic and conducting properties of LSMO film are determined by spin-up electronic density near the Fermi level, where 4-ZBNNR PDOS is equal to zero. Direct exchange interactions of electronic subsystems are responsible for the shrink of the gap in 4-ZBNNR PDOS up to 1.72 eV and dramatic reshape of both spin-up and spin-down channels of the fragment electronic subsystem.

The electronic structure calculations reveal no considerable change of LSMO electronic structure subsystem (Figures 5).

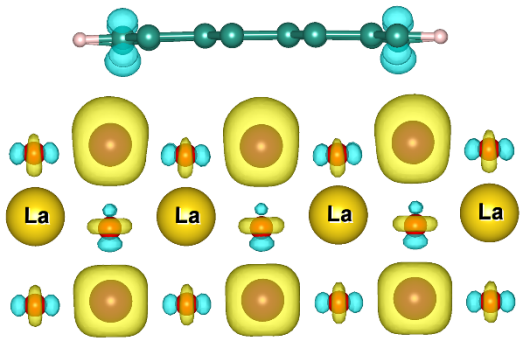

Figure 6. Spin density spatial distribution of 4-ZGNR/LSMO(001) interface. Blue and green colors correspond to spin-down and spin-up densities, respectively. Isosurface level is set to 0.01 e/Å^3.

Spatial spin density distribution of 4-ZGNR/LSMO(001) is presented in Figure 6. In contrast with Mn bulk ions (Mn_{bulk}), spatial distribution of partial spin-density of surface Mn ions ($Mn_{surface}$) is visibly shifted toward the interface. Mostly, spin density in 100% spin-polarized half-metallic LSMO fragment is localized on Mn and, in less extent, on oxygen ions. The Bader analysis[68–70] reveals 0.02 e, 0.41 e and 0.02 e charge transfer from LSMO support to 2D nanostructure for pentacene/LSMO(001), 4-ZGNR/LSMO(001) and 4-ZBNNR/LSMO heterostructures, respectively. Edge effect also causes visible differences of magnetic moments of surface and bulk ions: The $Mn_{surface}$(Mn_{bulk}) and O magnetic moments equal to 3.70-3.90

(3.22-3.29) μ_B and 0.05-0.07 μ_B, respectively. It is necessary to note that magnetic moments localized on La and Sr ions are very small (0.01and 0.005 μ_B, respectively).

Direct exchange interaction of LSMO and 4-ZGNR electronic subsystems leads to induced 0.064 μB magnetic moments localized on 4-ZGNR edge carbon atoms. The spatial spin density distribution map (Figure 6) directly demonstrates the localization of induced magnetic moments on the edge carbon atoms of 4-ZGNR, which would be responsible for transport properties of the composite.

Deposition of low-dimensional fragments also change the magnetic moments of surface manganese ions through the direct exchange mechanism. For example, η^1 coordinated Mn ions bear 3.70 μ_B instead of 3.89 μ_B for clean surface. This phenomenon can be caused by strong exchange interactions of C_p_z and $Mn\_d_{z^2}$ orbitals with positive net spin on ZGNR, which means strong spin injection at the interface. Direct exchange interactions of LSMO and 4-ZGNR electronic subsystems lead to induced 0.064 μ_B magnetic moments localized on 4-ZGNR edge carbon atoms. The spatial spin density distribution map (Figure 6) directly demonstrates the localization of induced magnetic moments on the edge carbon atoms of 4-ZGNR, which are responsible for nanoribbon transport properties. Magnetic moments localized on La and Sr ions are very small (0.016 and 0.005 μ_B, respectively). The average magnetic moments of N atoms in the 4-ZBNNR/LSMO lie in the range of 0.005 – 0.026 μ_B, whereas B atoms reveal 0 μ_B.

Conclusions

The atomic and electronic structure and induced spin polarization of pentacene molecule, 4-ZGNR and 4-ZBNNR at MnO-terminated LSMO(001) surface was studied using *ab initio* GGA+U approach. It was found that the interface formation leads to distinctive lift of spin degeneracy (pentacene and 4-ZBNNR) or asymmetric shift of spin-up and spin-down bands (4-ZGNR) through the direct exchange with Mn ions at LSMO surface, localization of 2D electron gas between the heterostructure fragments and charge transfer of 0.02 – 0.41 *e* from LSMO substrate to quantum well region. It was found that in all heterostructures the weak dispersion interactions are responsible for the binding of the fragments. The interactions of 2D fragments with LSMO lead to visible deformations of the π-conjugated fragments and LSMO surface layer. The direct exchange interactions between the electronic subsystems of 100% spin-polarized LSMO and ZGNR lead to transition of ZGNR narrow-band gap antiferromagnetic electronic structure to 100% spin-polarized half-metal. The spin polarization of 4-ZGNR keeps the same sign of polarization as the substrate resulting in strong spin transport and large magnetoresistance. Direct exchange interactions between p_z orbitals of nanofragments and d_{z^2} orbitals of Mn top layer cause a decreasing of the magnetic moments of Mn ions. Our results demonstrate a possibility to use MnO-terminated 4-ZGNR/LSMO(001) heterostructure as half-metallic fragments for promising spin-related applications.

Acknowledgements: We acknowledge the Siberian Supercomputer Center (SSCC) of SB RAS, Novosibirsk; the Joint Supercomputer Center of RAS, Moscow and the ICC of Novosibirsk State University for providing the computing resources. Russian Science Foundation (Grant No 14-13-00139) supported the work of Russian team.

References

[1] E.L. Nagaev, Lanthanum manganites and other giant-magnetoresistance magnetic conductors, Physics-Uspekhi. 39 (1996) 781–805. doi:10.1070/PU1996v039n08ABEH000161.

[2] et. al. Perkalina T.M., Kotjuzhansky B. Ya., Shapiro A.Ya., Cherkezyan S.A. Fiz. Tverd. Tela. 32 (1990) 1242.

[3] M.A. Ruderman, C. Kittel, Indirect Exchange Coupling of Nuclear Magnetic Moments by Conduction Electrons, Phys. Rev. 96 (1954) 99–102. doi:10.1103/PhysRev.96.99.

[4] T. Kasuya, A Theory of Metallic Ferro- and Antiferromagnetism on Zener's Model, Prog. Theor. Phys. 16 (1956) 45–57. doi:10.1143/PTP.16.45.

[5] K. Yosida, Magnetic Properties of Cu-Mn Alloys, Phys. Rev. 106 (1957) 893–898. doi:10.1103/PhysRev.106.893.

[6] E.L. Nagaev, Phase-separation mechanism for giant magnetoresistance of lanthanum manganites, Phys. Lett. A. 218 (1996) 367–372. doi:10.1016/0375-9601(96)00372-6.

[7] S. Tamura, Magnetic measurements of $(La_{0.8}Ca_{0.2})MnO_{3+y}$ by the Faraday method, Phys. Lett. A. 78 (1980) 401–403. doi:10.1016/0375-9601(80)90407-7.

[8] T. Yokota, S. Murata, M. Gomi, Electric field-induced magnetic changes in $La_{0.7}Sr_{0.3}MnO_3$ thin film using electric field-induced resistance phenomenon, Appl. Phys. Lett. 102 (2013) 152404. doi:10.1063/1.4802483.

[9] W.E. Pickett, D.J. Singh, Magnetoelectronic and Magnetostructural Coupling in the $La_{1-x}Ca_xMnO_3$ System, Phys. Rev. B. 53 (1996) 1146–1160. doi:10.1209/0295-5075/32/9/010.

[10] E. Cobas, A.L. Friedman, O.M.J. Van't Erve, J.T. Robinson, B.T. Jonker, Graphene as a tunnel barrier: graphene-based magnetic tunnel junctions., Nano Lett. 12 (2012) 3000–4. doi:10.1021/nl3007616.

[11] W.J.M. Naber, S. Faez, W.G. van der Wiel, Organic spintronics, J. Phys. D. Appl. Phys. 40 (2007) R205–R228. doi:10.1088/0022-3727/40/12/R01.

[12] N. Tombros, C. Jozsa, M. Popinciuc, H.T. Jonkman, B.J. van Wees, Electronic spin transport and spin precession in single graphene layers at room temperature, Nature. 448 (2007) 571–574. doi:10.1038/nature06037.

[13] A.K. Geim, K.S. Novoselov, The rise of graphene., Nat. Mater. 6 (2007) 183–91. doi:10.1038/nmat1849.

[14] M. Shiraishi, T. Ikoma, Molecular spintronics, Phys. E Low-Dimensional Syst. Nanostructures. 43 (2011) 1295–1317. doi:10.1016/j.physe.2011.02.010.

[15] A.A. Kuzubov, E.A. Kovaleva, P. Avramov, A. V. Kuklin, N.S. Mikhaleva, F.N. Tomilin, S. Sakai, S. Entani, Y. Matsumoto, H. Naramoto, Contact-induced spin polarization in BNNT(CNT)/TM (TM=Co, Ni) nanocomposites, J. Appl. Phys. 116 (2014) 84309. doi:10.1063/1.4894157.

[16] E.A. Kovaleva, A.A. Kuzubov, P.V. Avramov, A.V. Kuklin, N.S. Mikhaleva, P.O. Krasnov, Characterization of LSMO/C_{60} spinterface by first-principle calculations, 37 (2016) 55-60. doi:10.1016/j.orgel.2016.06.021.

[17] Z.H. Xiong, D. Wu, Z.V. Vardeny, J. Shi, Giant magnetoresistance in organic spin-valves, Nature. 427 (2004) 821–824. doi:10.1038/nature02277.1.

[18] S. Sakai, I. Sugai, S. Mitani, K. Takanashi, Y. Matsumoto, H. Naramoto, P. V. Avramov, S. Okayasu, Y. Maeda, Giant tunnel magnetoresistance in codeposited fullerene-cobalt films in the low bias-voltage regime, Appl. Phys. Lett. 91 (2007) 242104. doi:10.1063/1.2822397.

[19] X. Chen, N. Wu, J. Strozier, A. Ignatiev, Spatially extended nature of resistive switching in perovskite oxide thin films, Appl. Phys. Lett. 89 (2006) 63507. doi:10.1063/1.2236213.

[20] J.-H. Park, E. Vescovo, H.-J. Kim, C. Kwon, R. Ramesh, T. Venkatesan, Direct evidence for a half-metallic ferromagnet, 392 (1998) 794–796. doi:10.1038/33883.

[21] M. Viret, J. Nassar, M. Drouet, J.. Contour, C. Fermon, A. Fert, Spin polarised tunnelling as a probe of half metallic ferromagnetism in mixed-valence manganites, J. Magn. Magn.

Mater. 198–199 (1999) 1–5. doi:10.1016/S0304-8853(98)00589-7.
[22] C. Barraud, P. Seneor, R. Mattana, S. Fusil, K. Bouzehouane, C. Deranlot, P. Graziosi, L. Hueso, I. Bergenti, V. Dediu, F. Petroff, A. Fert, Unravelling the role of the interface for spin injection into organic semiconductors, Nat. Phys. 6 (2010) 615–620. doi:10.1038/nphys1688.
[23] V. Dediu, L.E. Hueso, I. Bergenti, A. Riminucci, F. Borgatti, P. Graziosi, C. Newby, F. Casoli, M.P. De Jong, C. Taliani, Y. Zhan, Room-temperature spintronic effects in Alq3 - based hybrid devices, Phys. Rev. B - Condens. Matter Mater. Phys. 78 (2008). doi:10.1103/PhysRevB.78.115203.
[24] B.B. Chen, Y. Zhou, S. Wang, Y.J. Shi, H.F. Ding, D. Wu, Giant magnetoresistance enhancement at room-temperature in organic spin valves based on $La_{0.67}Sr_{0.33}MnO_3$ electrodes, Appl. Phys. Lett. 103 (2013) 72402. doi:10.1063/1.4818614.
[25] Y. Mao, J. Yuan, J. Zhong, Density functional calculation of transition metal adatom adsorption on graphene., J. Phys. Condens. Matter. 20 (2008) 115209. doi:10.1088/0953-8984/20/11/115209.
[26] A.H. Davis, K. Bussmann, Organic luminescent devices and magnetoelectronics, J. Appl. Phys. 93 (2003) 7358. doi:10.1063/1.1540174.
[27] I. Bergenti, V. Dediu, E. Arisi, T. Mertelj, M. Murgia, A. Riminucci, G. Ruani, M. Solzi, C. Taliani, Spin polarised electrodes for organic light emitting diodes, Org. Electron. 5 (2004) 309–314. doi:10.1016/j.orgel.2004.10.004.
[28] M. Rocci, J. Tornos, A. Rivera-Calzada, Z. Sefrioui, M. Clement, E. Iborra, C. Leon, J. Santamaria, Resistive switching in manganite/graphene hybrid planar nanostructures, Appl. Phys. Lett. 104 (2014) 102408. doi:10.1063/1.4868426.
[29] F. Li, T. Li, X. Guo, Vertical graphene spin valves based on $La_{(2/3)}Sr_{(1/3)}MnO_{(3)}$ electrodes., ACS Appl. Mater. Interfaces. 6 (2014) 1187–92. doi:10.1021/am404866r.
[30] L.E. Hueso, J.M. Pruneda, V. Ferrari, G. Burnell, J.P. Valdés-Herrera, B.D. Simons, P.B. Littlewood, E. Artacho, A. Fert, N.D. Mathur, Transformation of spin information into large electrical signals using carbon nanotubes., Nature. 445 (2007) 410–3. doi:10.1038/nature05507.
[31] H. Xie, D. Niu, L. Lyu, H. Zhang, Y. Zhang, P. Liu, P. Wang, D. Wu, Y. Gao, Evolution of the electronic structure of $C_{60}/La_{0.67}Sr_{0.33}MnO_3$ interface, Appl. Phys. Lett. 108 (2016) 11603. doi:10.1063/1.4939457.
[32] F.J. Wang, C.G. Yang, Z.V. Vardeny, X.G. Li, Spin response in organic spin valves based on $La_{2/3}Sr_{1/3}MnO_3$ electrodes, Phys. Rev. B. 75 (2007) 245324. doi:10.1103/PhysRevB.75.245324.
[33] V.A. Dediu, L.E. Hueso, I. Bergenti, C. Taliani, Spin routes in organic semiconductors., Nat. Mater. 8 (2009) 707–16. doi:10.1038/nmat2510.
[34] P. Graziosi, A. Riminucci, M. Prezioso, C. Newby, D. Brunel, I. Bergenti, D. Pullini, D. Busquets-Mataix, M. Ghidini, V.A. Dediu, Pentacene thin films on ferromagnetic oxide: Growth mechanism and spintronic devices, Appl. Phys. Lett. 105 (2014) 22401. doi:10.1063/1.4890328.
[35] K. Toyoda, I. Hamada, K. Lee, S. Yanagisawa, Y. Morikawa, Density functional theoretical study of pentacene/noble metal interfaces with van der Waals corrections: vacuum level shifts and electronic structures., J. Chem. Phys. 132 (2010) 134703. doi:10.1063/1.3373389.
[36] Y.-H. Chu, C.-H. Hsu, C.-I. Lu, H.-H. Yang, T.-H. Yang, C.-H. Luo, K.-J. Yang, S.-H. Hsu, G. Hoffmann, C.-C. Kaun, M.-T. Lin, Spin-Dependent Molecule Symmetry at a Pentacene-Co Spinterface., ACS Nano. 9 (2015) 7027–32. doi:10.1021/acsnano.5b03117.
[37] M.V. Kamalakar, A. Dankert, J. Bergsten, T. Ive, S.P. Dash, Enhanced tunnel spin injection into graphene using chemical vapor deposited hexagonal boron nitride., Sci. Rep. 4 (2014) 6146. doi:10.1038/srep06146.
[38] M.V. Kamalakar, A. Dankert, P.J. Kelly, S.P. Dash, Inversion of Spin Signal and Spin

Filtering in Ferromagnet|Hexagonal Boron Nitride-Graphene van der Waals Heterostructures, Sci. Rep. 6 (2016) 21168. doi:10.1038/srep21168.
[39] Y.-W. Son, M.L. Cohen, S.G. Louie, Energy Gaps in Graphene Nanoribbons, Phys. Rev. Lett. 98 (2007) 89901. doi:10.1103/PhysRevLett.98.089901.
[40] L. Yang, M.L. Cohen, S.G. Louie, Magnetic edge-state excitons in zigzag graphene nanoribbons, Phys. Rev. Lett. 101 (2008) 186401. doi:10.1103/PhysRevLett.101.186401.
[41] M. Topsakal, H. Sevinçli, S. Ciraci, Spin confinement in the superlattices of graphene ribbons, Appl. Phys. Lett. 92 (2008) 173118. doi:10.1063/1.2919525.
[42] W. Zhang, Voltage-driven spintronic logic gates in graphene nanoribbons., Sci. Rep. 4 (2014) 6320. doi:10.1038/srep06320.
[43] Q.-Q. Sun, L.-H. Wang, W. Yang, P. Zhou, P.-F. Wang, S.-J. Ding, D.W. Zhang, Atomic scale investigation of a graphene nano-ribbon based high efficiency spin valve., Sci. Rep. 3 (2013) 2921. doi:10.1038/srep02921.
[44] Y. Ni, K. Yao, H. Fu, G. Gao, S. Zhu, S. Wang, Spin seebeck effect and thermal colossal magnetoresistance in graphene nanoribbon heterojunction., Sci. Rep. 3 (2013) 1380. doi:10.1038/srep01380.
[45] J. Baringhaus, M. Ruan, F. Edler, A. Tejeda, M. Sicot, A. Taleb-Ibrahimi, A.-P. Li, Z. Jiang, E.H. Conrad, C. Berger, C. Tegenkamp, W.A. de Heer, Exceptional ballistic transport in epitaxial graphene nanoribbons., Nature. 506 (2014) 349–54. doi:10.1038/nature12952.
[46] A.H. Castro Neto, N.M.R. Peres, K.S. Novoselov, A.K. Geim, The electronic properties of graphene, Rev. Mod. Phys. 81 (2009) 109–162. doi:10.1103/RevModPhys.81.109.
[47] P.E. Blöchl, Projector augmented-wave method, Phys. Rev. B. 50 (1994) 17953–17979. doi:10.1103/PhysRevB.50.17953.
[48] V.I. Anisimov, J. Zaanen, O.K. Andersen, Band theory and Mott insulators: Hubbard U instead of Stoner I, Phys. Rev. B. 44 (1991) 943–954. doi:10.1103/PhysRevB.44.943.
[49] S.L. Dudarev, S.Y. Savrasov, C.J. Humphreys, A.P. Sutton, Electron-energy-loss spectra and the structural stability of nickel oxide: An LSDA+U study, Phys. Rev. B. 57 (1998) 1505–1509. doi:10.1103/PhysRevB.57.1505.
[50] J.P. Perdew, K. Burke, M. Ernzerhof, Generalized Gradient Approximation Made Simple, Phys. Rev. Lett. 77 (1996) 3865–3868. doi:10.1103/PhysRevLett.77.3865.
[51] S. Grimme, Semiempirical GGA-type density functional constructed with a long-range dispersion correction., J. Comput. Chem. 27 (2006) 1787–99. doi:10.1002/jcc.20495.
[52] C. Ma, Z. Yang, S. Picozzi, Ab initio electronic and magnetic structure in $La_{(0.66)}Sr_{(0.33)}MnO_{(3)}$: strain and correlation effects., J. Phys. Condens. Matter. 18 (2006) 7717–28. doi:10.1088/0953-8984/18/32/019.
[53] S. Picozzi, C. Ma, Z. Yang, R. Bertacco, M. Cantoni, A. Cattoni, D. Petti, S. Brivio, F. Ciccacci, Oxygen vacancies and induced changes in the electronic and magnetic structures of $La_{0.66}Sr_{0.33}MnO_3$: A combined ab initio and photoemission study, Phys. Rev. B. 75 (2007) 94418. doi:10.1103/PhysRevB.75.094418.
[54] B. Zheng, N. Binggeli, Influence of the interface atomic structure on the magnetic and electronic properties of $La_{2/3}Sr_{1/3}MnO_3/SrTiO_3$ (001) heterojunctions, Phys. Rev. B. 82 (2010) 245311. doi:10.1103/PhysRevB.82.245311.
[55] H.J. Monkhorst, J.D. Pack, Special points for Brillouin-zone integrations, Phys. Rev. B. 13 (1976) 5188–5192. doi:10.1103/PhysRevB.13.5188.
[56] G. Kresse, J. Furthmüller, Efficient iterative schemes for ab initio total-energy calculations using a plane-wave basis set, Phys. Rev. B. 54 (1996) 11169–11186. doi:10.1103/PhysRevB.54.11169.
[57] G. Kresse, J. Hafner, Ab initio molecular dynamics for liquid metals, Phys. Rev. B. 47 (1993) 558–561. doi:10.1103/PhysRevB.47.558.
[58] M.C. Martin, G. Shirane, Y. Endoh, K. Hirota, Y. Moritomo, Y. Tokura, Magnetism and structural distortion in the $La_{0.7}Sr_{0.3}MnO_3$ metallic ferromagnet, Phys. Rev. B. 53 (1996)

14285–14290. doi:10.1103/PhysRevB.53.14285.
[59] F. Tsui, M.C. Smoak, T.K. Nath, C.B. Eom, Strain-dependent magnetic phase diagram of epitaxial $La_{0.67}Sr_{0.33}MnO_3$ thin films, Appl. Phys. Lett. 76 (2000) 2421. doi:10.1063/1.126363.
[60] P. Yu, W. Luo, D. Yi, J.X. Zhang, M.D. Rossell, C.-H. Yang, L. You, G. Singh-Bhalla, S.Y. Yang, Q. He, Q.M. Ramasse, R. Erni, L.W. Martin, Y.H. Chu, S.T. Pantelides, S.J. Pennycook, R. Ramesh, Interface control of bulk ferroelectric polarization, Proc. Natl. Acad. Sci. 109 (2012) 9710–9715. doi:10.1073/pnas.1117990109.
[61] J.-L. Maurice, D. Imhoff, J.-P. Contour, C. Colliex, Interfaces in {100} epitaxial heterostructures of perovskite oxides, Philos. Mag. 86 (2006) 2127–2146. doi:10.1080/14786430600640460.
[62] M. Yoshimoto, H. Maruta, T. Ohnishi, K. Sasaki, H. Koinuma, In situ determination of the terminating layer of $La_{0.7}Sr_{0.3}MnO_3$ thin films using coaxial impact-collision ion scattering spectroscopy, Appl. Phys. Lett. 73 (1998) 187. doi:10.1063/1.121750.
[63] H. Boschker, J. Verbeeck, R. Egoavil, S. Bals, G. van Tendeloo, M. Huijben, E.P. Houwman, G. Koster, D.H.A. Blank, G. Rijnders, Preventing the Reconstruction of the Polar Discontinuity at Oxide Heterointerfaces, Adv. Funct. Mater. 22 (2012) 2235–2240. doi:10.1002/adfm.201102763.
[64] A.Y. Petrov, X. Torrelles, A. Verna, H. Xu, A. Cossaro, M. Pedio, J. Garcia-Barriocanal, G.R. Castro, B.A. Davidson, Surface octahedral distortions and atomic design of perovskite interfaces., Adv. Mater. 25 (2013) 4043–8. doi:10.1002/adma.201301841.
[65] L. Poggini, S. Ninova, P. Graziosi, M. Mannini, V. Lanzilotto, B. Cortigiani, L. Malavolti, F. Borgatti, U. Bardi, F. Totti, I. Bergenti, V.A. Dediu, R. Sessoli, A Combined Ion Scattering, Photoemission, and DFT Investigation on the Termination Layer of a $La_{0.7}Sr_{0.3}MnO_3$ Spin Injecting Electrode, J. Phys. Chem. C. 118 (2014) 13631–13637. doi:10.1021/jp5026619.
[66] Z. Liao, M. Huijben, Z. Zhong, N. Gauquelin, S. Macke, R.J. Green, S. Van Aert, J. Verbeeck, G. Van Tendeloo, K. Held, G.A. Sawatzky, G. Koster, G. Rijnders, Controlled lateral anisotropy in correlated manganite heterostructures by interface-engineered oxygen octahedral coupling, Nat. Mater. 15 (2016) 425–431. doi:10.1038/nmat4579.
[67] Q. Zhang, L. Yin, W. Mi, X. Wang, Large Spatial Spin Polarization at Benzene/$La_{2/3}Sr_{1/3}MnO_3$ Spinterface: Toward Organic Spintronic Devices, J. Phys. Chem. C. 120 (2016) 6156–6164. doi:10.1021/acs.jpcc.6b01165.
[68] G. Henkelman, A. Arnaldsson, H. Jónsson, A fast and robust algorithm for Bader decomposition of charge density, Comput. Mater. Sci. 36 (2006) 354–360. doi:10.1016/j.commatsci.2005.04.010.
[69] E. Sanville, S.D. Kenny, R. Smith, G. Henkelman, Improved grid-based algorithm for Bader charge allocation, J. Comput. Chem. 28 (2007) 899–908. doi:10.1002/jcc.20575.
[70] W. Tang, E. Sanville, G. Henkelman, A grid-based Bader analysis algorithm without lattice bias., J. Phys. Condens. Matter. 21 (2009) 84204. doi:10.1088/0953-8984/21/8/084204.